Role of short- and long-range ordering on diffusion in Ni-Al alloys

Jon Gabriel Goiri, Sanjeev Krishna Kolli, and Anton Van der Ven

Phys. Rev. Materials **3**, 093402 — Published 3 September 2019

DOI: 10.1103/PhysRevMaterials.3.093402

The role of short- and long-range ordering on diffusion in Ni-Al alloys

Jon Gabriel Goiri, Sanjeev Krishna Kolli, and Anton Van der Ven*
Materials Department, University of California Santa Barbara
(Dated: August 12, 2019)

The varying degrees of short- and long-range order exhibited by multi-component solids complicates a first-principles calculation of non-dilute diffusion coefficients. Temporal and spatial variations in the local degree of order affect the migration barriers of individual hops and can result in strong correlations between successive hops that ultimately affect macroscopic transport coefficients. Here we report on a first-principles study of diffusion in Ni-rich Ni-Al alloys. We used cluster expansion Hamiltonians to describe the energies of the end states and migration barriers of each hop. Kinetic Monte Carlo simulations were performed to calculate macroscopic transport coefficients. Variations in the degree of ordering are shown to play a significant role in affecting diffusion coefficients. While Al has a higher mobility than Ni in the disordered Ni-rich fcc solid solution, it becomes significantly less mobile in the ordered $L1_2$ γ' phase due to strong thermodynamic tendencies that keep Al trapped to disconnected sublattice sites.

I. INTRODUCTION

Solid state diffusion is an important property for many applications. It determines, for example, how fast a battery or a fuel cell can operate[1–4]. Diffusion also plays a central role during the processing of materials, where diffusional phase transformations are often exploited to achieve a particular microstructure[5–7]. Precipitation reactions, for example, depend sensitively on the rates with which the different components of an alloy diffuse[8]. Long-term stability of alloy microstructures with respect to coarsening processes are also sensitive to the mobilities of the constituents of the alloy[9–11]. Numerous structural and functional applications rely on artificial multi-layers that are susceptible to degradation due to interdiffusion[12].

First-principles approaches are now commonly used to calculate diffusion coefficients in dilute alloys[13–26]. Diffusion coefficients are more challenging to calculate in non-dilute alloys, however, due to the wide variety of local environments that hopping atoms encounter as they migrate through a concentrated crystal[27–38] Most solid solutions, while disordered, still continue to exhibit local short-range order that fluctuates spatially throughout the solid. Ordered compounds, in contrast, are characterized by long-range order, but often also exhibit some local disorder due to the presence of anti-site defects that accommodate off-stoichiometry or emerge from thermal excitations. These spatial and temporal variations in local order affect the activation barriers, ΔE, of diffusing atoms along their trajectories. They also often result in correlations between successive hops that ultimately affect macroscopic diffusion coefficients[33,39].

The aim of this study is to establish the extent with which migration barriers in substitutional alloys can depend on local ordering around the activated state and how this manifests itself in macroscopic transport coefficients. We combine first-principles electronic structure calculations with cluster expansion approaches[40,41] and kinetic Monte Carlo simulations[42] to predict macroscopic transport coefficients. As a model system, we consider the FCC phases of the Ni-Al binary as they feature a rich variety of long and short-range order. The Ni-Al binary includes the Ni-rich FCC solid solution, also referred to as γ, and the γ'-Ni_3Al phase having the $L1_2$ ordering on FCC[43]. These phases form the basis of most modern jet engine turbine blades[44,45]. We find that variations in local alloy concentration and ordering can have a strong influence on the migration barriers of Al hops, but much less so for Ni hops. The diffusion coefficient of Al is predicted to be higher than that of Ni in the disordered γ phase, but this is reversed in the ordered γ'-Ni_3Al phase where Al remains locked on the disconnected sublattice of the $L1_2$ ordering. Our study demonstrates the importance of varying degrees of long and short-range order on diffusion coefficients.

II. THEORETICAL FORMALISM

This section summarizes various phenomenological metrics of atomic mobility in substitutional alloys and describes how they can be calculated starting with an atomic description of hop frequencies. We make a distinction between perfect crystals, where the number of vacancies are conserved, and solids containing a sufficient number of vacancy sources and sinks to ensure local equilibrium in the vacancy concentration. The two extremes lead to different sets of diffusion coefficients.

A. The case of a perfect crystal of a binary substitutional alloy

We focus on the Ni rich fcc-based phases of the Ni-Al binary. These phases accommodate dilute concentrations of vacancies that can mediate substitutional diffusion. In an actual alloy, extended defects such as dislocations and grain boundaries act as sources and sinks for vacancies. In this section, we review metrics of substitutional diffusion in crystals where no such sources and sinks are present, and where the number of sites of the crystal, M,

and the total number of vacancies, N_{Va}, is conserved. We will refer to these solids as "perfect crystals," noting that, while they do not contain dislocations or grain boundaries, they still contain vacancies.

Imbalances in the chemical potentials of mobile species act as thermodynamic driving forces for atomic diffusion. Chemical potentials can be extracted from the Gibbs free energy, G, of the alloy, which is a function of the temperature, T, pressure, P, and the number of atoms N_{Ni} and N_{Al}. The free energy of a perfect crystal can be normalized by the number of sites in the crystal

$$g\left(T, P, x_{\mathrm{Ni}}, x_{\mathrm{Al}}\right) = \frac{G}{M} \tag{1}$$

where x_{Ni} and x_{Al} are the Ni and Al atom fractions relative to the number of sites in the crystal, M (such that $x_{\mathrm{Ni}} + x_{\mathrm{Al}} + x_{\mathrm{Va}} = 1$).

Diffusion in a perfect crystal is driven by gradients of "diffusion potentials", defined as[35,46–48]

$$\tilde{\mu}_i = \frac{\partial g}{\partial x_i} = \mu_i - \mu_{\mathrm{Va}} \tag{2}$$

The diffusion potential of a species i is equal to the difference in the chemical potential of i, $\mu_i = (\partial G/\partial N_i)_{T,P,N_{j\neq i}}$, and the vacancy chemical potential, $\mu_{\mathrm{Va}} = (\partial G/\partial N_{\mathrm{Va}})_{T,P,N_{j\neq Va}}$. Each $\tilde{\mu}_i$ can be viewed as the change in free energy of the alloy as an atom of type i is added to the solid at the expense of a vacancy (holding the number of crystal sites M constant).

Diffusion fluxes within a perfect crystal are related to the gradients of diffusion potentials according to

$$\begin{bmatrix} \vec{J}_{\mathrm{Ni}} \\ \vec{J}_{\mathrm{Al}} \end{bmatrix} = -\begin{bmatrix} L_{\mathrm{Ni,Ni}} & L_{\mathrm{Ni,Al}} \\ L_{\mathrm{Al,Ni}} & L_{\mathrm{Al,Al}} \end{bmatrix} \begin{bmatrix} \nabla\tilde{\mu}_{\mathrm{Ni}} \\ \nabla\tilde{\mu}_{\mathrm{Al}} \end{bmatrix} \tag{3}$$

where the L_{ij} refer to Onsager transport coefficients[1,47,49]. Note that only the fluxes for Ni and Al need be accounted for since $\vec{J}_{\mathrm{Va}} + \vec{J}_{\mathrm{Ni}} + \vec{J}_{\mathrm{Al}} = 0$ when the number of sites M is conserved.

Kubo-Green linear response methods can be used to relate the phenomenological Onsager transport coefficients of eq. (3) to fluctuations that occur at the atomic scale in equilibrium[50–52]. At finite temperature, atoms will be in continuous motion, migrating from one site to the next through atom-vacancy exchanges. For a crystalline solid,[50,52]

$$L_{ij} = \frac{1}{\Omega k_B T}\tilde{L}_{ij} \tag{4}$$

with

$$\tilde{L}_{ij} = \frac{\langle\left(\sum_\zeta \Delta\vec{R}_i^\zeta(t)\right)\left(\sum_\zeta \Delta\vec{R}_j^\zeta(t)\right)\rangle}{(2d)tM} \tag{5}$$

Here, k_B is the Boltzmann constant, T is the temperature, Ω is the volume per substitutional site, M is the number of sites in the crystal, and d is the dimensionality of the substitutional network (e.g. for a 3-dimensional substitutional network $d = 3$, while a layered material would have $d = 2$). The vectors $\Delta\vec{R}_i^\zeta$ connect the end points of the trajectory of atom ζ being a species of type i after the elapse of a time t. The brackets $\langle\,\rangle$ denote ensemble averages at equilibrium. Note that eq. (5) satisfies the Onsager reciprocity relations[53], which require that $L_{ij} = L_{ji}$.

Other purely kinetic quantities can be defined in terms of the $\Delta\vec{R}_i^\zeta$, including correlation factors and tracer diffusion coefficients. The correlation factor f_i of a species i is defined as[48,54]

$$f_i = \frac{\langle\Delta\vec{R}_i^2\rangle}{N_\tau\Delta\vec{r}^{\,2}} \tag{6}$$

where N_τ is equal to the number of hops and where $\Delta\vec{r}^{\,2}$ is the square of an elementary hop distance (e.g. nearest neighbor distance for nearest neighbor atom-vacancy exchanges). Correlation factors measure the degree with which correlations between successive hops affect atomic transport of individual atoms in a crystal. When an atom or vacancy performs a random walk, there are no correlations between successive hops and $f = 1$. When $f = 0$, every individual hop is exactly opposite the previous one. Tracer diffusion coefficients measure the diffusivity of tagged tracer atoms in the absence of chemical gradients and can be expressed as[48]

$$D_i^* = \frac{\langle\Delta\vec{R}_i^2\rangle}{2dt} \tag{7}$$

Gradients in chemical potential are not straightforward to measure experimentally. Flux expressions in terms of concentration gradients are more convenient, and can be derived from eq. (3) by chain rule differentiation of the chemical potentials. The flux expressions then take the form

$$\begin{bmatrix} \vec{J}_{\mathrm{Ni}} \\ \vec{J}_{\mathrm{Al}} \end{bmatrix} = -\begin{bmatrix} D_{\mathrm{Ni,Ni}} & D_{\mathrm{Ni,Al}} \\ D_{\mathrm{Al,Ni}} & D_{\mathrm{Al,Al}} \end{bmatrix} \begin{bmatrix} \nabla c_{\mathrm{Ni}} \\ \nabla c_{\mathrm{Al}} \end{bmatrix} \tag{8}$$

The matrix of diffusion coefficients, $\mathbf{D}$, are related to the Onsager transport coefficients according to[35]

$$\begin{bmatrix} D_{\mathrm{Ni,Ni}} & D_{\mathrm{Ni,Al}} \\ D_{\mathrm{Al,Ni}} & D_{\mathrm{Al,Al}} \end{bmatrix} = \begin{bmatrix} \tilde{L}_{\mathrm{Ni,Ni}} & \tilde{L}_{\mathrm{Ni,Al}} \\ \tilde{L}_{\mathrm{Al,Ni}} & \tilde{L}_{\mathrm{Al,Al}} \end{bmatrix} \begin{bmatrix} \tilde{\Theta}_{\mathrm{Ni,Ni}} & \tilde{\Theta}_{\mathrm{Ni,Al}} \\ \tilde{\Theta}_{\mathrm{Al,Ni}} & \tilde{\Theta}_{\mathrm{Al,Al}} \end{bmatrix} \tag{9}$$

The thermodynamic factor matrix, $\tilde{\mathbf{\Theta}}$, is proportional to the Hessian of the free energy[35]

$$\tilde{\mathbf{\Theta}} = \frac{1}{k_B T}\begin{bmatrix} \dfrac{\partial^2 g}{\partial x_{\mathrm{Ni}}\partial x_{\mathrm{Ni}}} & \dfrac{\partial^2 g}{\partial x_{\mathrm{Ni}}\partial x_{\mathrm{Al}}} \\ \dfrac{\partial^2 g}{\partial x_{\mathrm{Al}}\partial x_{\mathrm{Ni}}} & \dfrac{\partial^2 g}{\partial x_{\mathrm{Al}}\partial x_{\mathrm{Al}}} \end{bmatrix} \tag{10}$$

Similar to the Onsager transport coefficients, it is possible to relate the elements of the thermodynamic factor

matrix to fluctuations, this time in composition within the semi Grand Canonical ensemble according to[35]

$$\tilde{\Theta}_{ij}^{-1} = \frac{1}{M}\langle N_i N_j\rangle - \langle N_i\rangle\langle N_j\rangle \tag{11}$$

where the ensemble averages are performed in a crystal of M sites while holding the diffusion potentials $\tilde{\mu}_i$ constant.

Though $\mathbf{D}$ couples fluxes to gradients in concentration, the individual components of the matrix by themselves do not reveal the underlying physics of transport properties in a binary substitutional alloy where atomic hops are mediated by atom-vacancy exchanges. Key properties are embedded in the eigenvalues of $\mathbf{D}$. In the limit of a dilute vacancy concentration, the larger eigenvalue, λ^+, asymptotically converges to the vacancy diffusion coefficient, while the smaller eigenvalue, λ^-, becomes equal to an intermixing diffusion coefficient between Ni and Al[35,47]. Additional metrics can be defined in terms of the elements of $\mathbf{D}$ that measure the extent with which the alloy deviates from a kinetically ideal substitutional alloy, which is defined as an alloy that is not only thermodynamically ideal, but also has the property that the components of the alloy have identical atom-vacancy exchange frequencies. One such metric is defined as[35]

$$\phi = \frac{D_{\mathrm{Al,Ni}}}{D_{\mathrm{Ni,Al}} + D_{\mathrm{Al,Ni}}}, \tag{12}$$

and measures the fraction of Al that will exchange with a flux of vacancies. For a kinetically ideal substitutional alloy there is no bias in the atom-vacancy exchange frequency between the different components and ϕ becomes equal to the alloy concentration[35]. Any deviation from this value reveals a difference in the relative mobilities between the two components of the alloy. Another metric, defined as[35]

$$\delta = D_{\mathrm{Al,Al}} - D_{\mathrm{Ni,Ni}} + D_{\mathrm{Ni,Al}} - D_{\mathrm{Al,Ni}} \tag{13}$$

measures the degree with which a gradient between the Ni and Al concentrations, in the absence of a gradient in the vacancy concentration, induces a vacancy flux. δ reflects the alloy's susceptibility to the Kirkendall effect.

B. Vacancies at local equilibrium

Other diffusion metrics exist when there are sufficient vacancy sources and sinks to regulate an equilibrium vacancy concentration at each point within the alloy. In this scenario, the vacancy chemical potential μ_{Va} will be equal to zero throughout the solid, thereby imposing thermodynamic constraints on the chemical potentials of Ni and Al. This is a common assumption in analyses of substitutional diffusion and was first invoked by Darken[55]. Under this approximation, the flux expressions can be written as[35,48]

$$\vec{J}_i = -D_i \nabla c_i \tag{14}$$

where the self diffusion coefficients D_i are again a product of a kinetic and thermodynamic factor

$$D_i = \Lambda_i \Sigma \tag{15}$$

The kinetic factor for each species are related to the Onsager transport coefficients according to

$$\Lambda_i = \left(\frac{\tilde{L}_{i,i}}{x_i} - \frac{\tilde{L}_{i,j}}{x_j}\right) \tag{16}$$

The thermodynamic factors are the same for both species in the limit of a dilute vacancy concentration and can be calculated according to

$$\Sigma = \frac{x_i}{k_B T}\left(\frac{\mathrm{d}\mu_i}{\mathrm{d}x_i}\right)_{\mu_{\mathrm{Va}}=0} \tag{17}$$

The fluxes of eq. (14) are relative to the crystal frame of reference. However, in the presence of vacancy sources and sinks, such as dislocations and grain boundaries, the solid can become susceptible to the Kirkendall effect and single crystal regions may move relative to a fixed laboratory frame of reference. Interdiffusion between the two components of the alloy is usually measured in the laboratory frame of reference. The interdiffusion coefficient in the laboratory frame of reference can be expressed as[35,48]

$$\tilde{D} = \tilde{\Lambda}\Sigma \tag{18}$$

where for the Ni-Al binary

$$\tilde{\Lambda} = x_{\mathrm{Al}}\Lambda_{\mathrm{Ni}} + x_{\mathrm{Ni}}\Lambda_{\mathrm{Al}} \tag{19}$$

The interdiffusion coefficient $\tilde{D}$ is the analog of the perfect crystal intermixing coefficient, λ^-, but for a solid with sufficient vacancy sources and sinks to regulate an equilibrium vacancy concentration throughout the solid[35].

C. Atomistic description

Atoms of a substitutional alloy continuously exchange with a dilute concentration of vacancies and thereby wander throughout the crystal, even in thermodynamic equilibrium. The Kubo-Green expression of eq. (5) shows that the phenomenological transport coefficients can be calculated by tracking the trajectories $\Delta\vec{R}_i^{\zeta}$ of these mobile atoms. The trajectories $\Delta\vec{R}_i^{\zeta}$ are the result of many individual atom-vacancy exchanges that occur stochastically with frequencies that in a crystal can be approximated with transition state theory[56–59] according to

$$\Gamma = v^* \exp\left(\frac{-\Delta E}{k_B T}\right). \tag{20}$$

Here ΔE is the migration barrier for a hop and v^* is a vibrational prefactor. Within the harmonic approximation, the vibrational prefactor v^* is equal to the ratio

of the products of the normal mode frequencies in the activated and initial states[56]

$$v^* = \frac{\prod_{i=1}^{3N-3} v_i}{\prod_{k=1}^{3N-4} \tilde{v}_k} \tag{21}$$

where v and $\tilde{v}$ are the initial and activated state frequencies respectively and where N is the number of atoms in the crystal.

1. Cluster expansion representation of end state energies

Non dilute alloys exhibit varying degrees of short and long-range ordering as a function temperature and alloy composition. As atoms of an alloy migrate, they encounter a range of migration barriers due to fluctuations in the local degree of ordering along their trajectory. Modeling diffusion in concentrated substitutional alloys therefore requires an accurate description of the dependence of the energies of the end states and of the activated states on the local degree of short- and long-range order.

In this work, we use cluster expansion Hamiltonians[40,41,60–62] to describe the dependence of the energy of the solid on the particular arrangement of Ni, Al and vacancies over the sites of the FCC crystal. The energies of the end states of a hop in a Ni-Al alloy can be described with a ternary cluster expansion as each site of the crystal is either occupied by Ni, Al or a vacancy. For the Ni-rich alloy, it is convenient to assign two occupation variables to each crystal site i: p_i^{Al}, which is equal to 1 if the site is occupied by Al and zero otherwise and p_i^{Va}, which is 1 if the site is occupied by a vacancy and zero otherwise. The configurational state of a crystal of M sites is then uniquely determined by specifying the occupation variables at each site, $\vec{p} = \left(p_1^{Al}, p_1^{Va}, ..., p_i^{Al}, p_i^{Va}, ..., p_M^{Al}, p_M^{Va}\right)$. The energy of the crystal in any end state of a hop can be expressed as an expansion of polynomials of the occupation variables[40,62]

$$E(\vec{p}) = V_0 + \sum_{\alpha,\pi} V_{\alpha,\pi} \phi_{\alpha,\pi}(\vec{p}) \tag{22}$$

where each cluster basis functions, $\phi_{\alpha,\pi}(\vec{p})$, is a product of occupation variables belonging to a cluster of sites α according to

$$\phi_{\alpha,\pi}(\vec{p}) = \prod_{i \in \alpha} p_i^{\pi_i} \tag{23}$$

The clusters of sites, α, refer to point, pair, triplet etc. clusters, while the π denotes which occupation variable is to be assigned to each site in the cluster α. The $V_{\alpha,\pi}$ are constant expansion coefficients referred to as effective cluster interactions (ECI). The ECI of a cluster expansion Hamiltonian can be parameterized by training to a large number of energies for different alloy configurations $\vec{p}$ that have been calculated with a first principles electronic structure method such as density functional theory[43,63].

2. Cluster expansion description of activation barriers

The migration barrier for a particular hop is equal to the difference in energy between the activated state and the initial state of the hop. In FCC Ni-Al, there are two important hop types: a nearest neighbor Al-Va exchange and a nearest neighbor Ni-Va exchange. The migration barrier for each hop type, t, in a concentrated alloy depends on the local degree of ordering surrounding the sites participating in the hop. We denote this ordering as $\vec{p}_H = \vec{p} \setminus H$, which collects all the occupation variables of the crystal minus those residing on the hop cluster H. Migration barriers also depend on the direction of the hop, since the end states of most hops in a concentrated alloy will not have the same energy. This is schematically illustrated in fig. 1. The direction dependence of the migration barrier can be separated from the environment dependence by working with a Kinetically Resolved Activation (KRA) barrier, defined as[31]

$$\Delta E^{\mathrm{KRA}} = E^* - \frac{E_i + E_f}{2} \tag{24}$$

where E^* is the energy of the activated state, E_i is the energy of the initial state and E_f is the energy of the final state of the hop. The ΔE^{KRA}, while still a function of the hop type t and the hop environment $\vec{p}_H$, is independent of the hop direction. We denote this dependence as $\Delta E_t^{\mathrm{KRA}}(\vec{p}_H)$. For an atom-vacancy exchange mechanism on a nearest neighbor hop cluster, $\Delta E_t^{\mathrm{KRA}}(\vec{p}_H)$ simply reduces to an average of the forward and reverse hop activation barriers. In essence, the KRA separates the kinetic component of the hop from the thermodynamic end states.

As with the energies of the end states of a hop, the dependence of $\Delta E_t^{\mathrm{KRA}}$ on $\vec{p}_H$ can also be described with a (local) cluster expansion[31]

$$\Delta E_t^{\mathrm{KRA}}(\vec{p}_H) = K_0^t + \sum_{\alpha,\pi} K_\alpha^t \phi_{\alpha,\pi}(\vec{p}_H) \tag{25}$$

where the sum extends over clusters not including the hop cluster H. The expansion coefficients K_α^t can be determined by training to a large set of $\Delta E_t^{\mathrm{KRA}}(\vec{p}_H)$ values as calculated with a first-principles method. Each hop type t will have a separate cluster expansion.

Symmetry imposes constraints on the number of independent interaction coefficients. Diffusional hops in a substitutional solid can be approximated to occur in an infinite crystal far away from symmetry breaking defects such as dislocations and grain boundaries. The symmetric equivalence of two local environments around a particular hop type is then determined by a subgroup $\mathcal{L}$ of the crystal space group $\mathcal{S}$, obtained by taking the intersection of a hop symmetry group $\mathcal{H}$ with $\mathcal{S}$. For

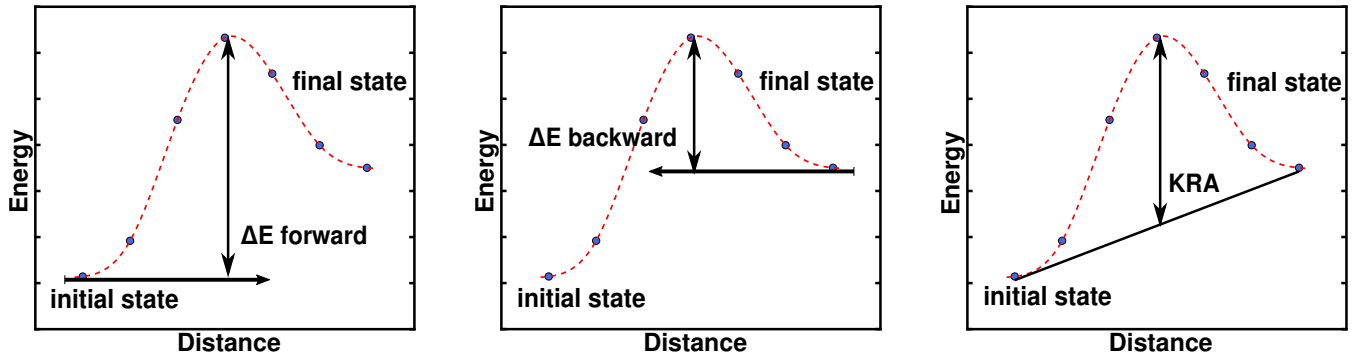

FIG. 1. The activation barrier for a forward hop (a) will differ from that of the reverse hop (b) if the energies of the end states are different. The kinetically resolved activation (KRA) barrier is independent of the hop direction as it is an average of the forward and backward activation barriers.

simple hops, such as the nearest neighbor atom-vacancy exchange mechanism, the hop symmetry group $\mathcal{H}$ reduces to the point group of the hop cluster (i.e. the point group that maps the nearest neighbor pair hop cluster onto itself). Any cluster function $\phi_{\alpha,\pi}(\vec{p})$ that can be mapped onto another cluster function $\phi_{\beta,\pi'}(\vec{p})$ using a symmetry operation from the subgroup $\mathcal{L} = \mathcal{H} \cap \mathcal{S}$ will have the same ECI (i.e. $K^t_{\alpha,\pi} = K^t_{\beta,\pi'}$).

Once cluster expansions for the end states of the hop (eq. (22)) and the KRA barrier for each of the hop types t have been parameterized using first-principles training data, it is possible to calculate the migration barrier for any local environment according to

$$\Delta E = E^* - E_i = \Delta E_t^{\mathrm{KRA}}(\vec{p}_H) + \frac{E(\vec{p}_f) - E(\vec{p}_i)}{2} \quad (26)$$

where $\vec{p}_f$ and $\vec{p}_i$ are the configurations of the crystal in the final and initial states, and where $\vec{p}_H$ is the configuration of the crystal minus the hop cluster sites (which remains unchanged during the hop).

III. COMPUTATIONAL DETAILS

The cluster expansions of the alloy and of the KRA barriers make it possible to calculate all the thermodynamic and kinetic quantities described in section II with Monte Carlo techniques. Grand Canonical Monte Carlo simulations applied to the crystal cluster expansion Hamiltonian, eq. (22), generate the necessary thermodynamic information to (i) construct an equilibrium temperature versus composition phase diagram, (ii) calculate the equilibrium vacancy concentration and (iii) estimate the elements of the thermodynamic factor matrix of eq. (10). Migration barriers in any alloy environment can be calculated by combining the alloy cluster expansion eq. (22) with the local cluster expansions for the KRAs, eq. (25), as in eq. (26). Atomic trajectories that arise from stochastic atom-vacancy exchanges can then be sampled with kinetic Monte Carlo simulations[42].

Cluster expansions were parameterized using large training sets of energies as calculated with density functional theory (DFT). All DFT calculations were performed with the generalized gradient approximation (GGA-PBE) using the projector augmented wave (PAW) pseudopotential method as implemented in the Vienna ab initio simulation package (VASP)[64–67]. A recursive approach[63] was used to parameterize the expansion coefficients of a ternary cluster expansion for the FCC Ni-Al-Va system by starting with a well optimized binary Ni-Al cluster expansion[43] and extending it to account for interactions between Al and vacancies. The vacancy concentration in the Ni-Al alloy is very dilute, allowing us to neglect interactions between vacancies. The binary Ni-Al cluster expansion[43] was extended by fitting Al-vacancy interaction coefficients using 50 DFT energies of configurations containing a vacancy within a 107 atom supercell ($3 \times 3 \times 3$ conventional cubic FCC unit cells) in either $L1_2$ derived configurations or in various Ni-rich FCC configurations. At this size, convergence errors due to interactions between periodic images were found to be below 25meV per vacancy (based on a comparison of calculations performed in $4 \times 4 \times 4$ conventional FCC cells). A k-point mesh of $4 \times 4 \times 4$, with a smearing parameter of 0.2eV, was used. Calculations were performed spin polarized with ferromagnetic ordering initialized in each supercell and with a plane wave cutoff energy of 560eV.

Two local cluster expansions were constructed to describe the dependence of $\Delta E_t^{\mathrm{KRA}}(\vec{p}_H)$ on local ordering for the Ni-vacancy and Al-vacancy exchange hop types t. Each of the local cluster expansions were fit to first-principles KRA barriers, calculated for configurations in Ni rich FCC and $L1_2$. Diffusion barriers for low symmetry hops were calculated in 107 atom supercells ($3 \times 3 \times 3$ of the conventional cubic FCC unit cell) with DFT using the nudged elastic band[68] (NEB) method as implemented in VASP. The volume of all images in each NEB calculation was held constant, but the ionic positions were allowed to relax. A total of 7 images were considered in

each NEB calculation, which included the two end states of each hop. For hops in high symmetry environments with a mirror plane perpendicularly bisecting the hop cluster, only a single supercell calculation is necessary, provided the migrating atom is placed in the mirror plane of a high-symmetry, prerelaxed crystal to ensure that the migrating atom remains at the saddle point during relaxation.

Vibrational prefactors, defined by eq. (21), were approximated by calculating vibrational frequencies of Ni and Al within a 31 atom Ni supercell. Supercells with either Ni or Al in both the equilibrium and activated state were first completely relaxed. Vibrational frequencies for both the equilibrium and activated states were then determined from the Hessian matrix as calculated with VASP. This yielded $\nu^*_{\mathrm{Ni}} = 3.11\,\mathrm{THz}$, and $\nu^*_{\mathrm{Al}} = 4.39\,\mathrm{THz}$. We used these values for all hop environments in subsequent kinetic Monte Carlo simulations.

Grand canonical Monte Carlo simulations were performed using the CASM[62,69–71] software package to calculate the binary temperature versus composition phase diagram and the equilibrium vacancy concentration as a function of alloy composition. The equilibrium vacancy concentration was determined by setting $\mu_{\mathrm{Va}} = 0$. This thermodynamic boundary condition is equivalent to minimizing the Gibbs free energy of the alloy with respect to the vacancy concentration and mimics the role of extended defects such as dislocations and grain boundaries that act as sources and sinks for vacancies. The equilibrium vacancy concentration in actual crystals cannot be controlled experimentally and is instead regulated by these imperfections. We also tracked the fluctuations in composition during the Monte Carlo simulations to calculate the thermodynamic factor according to eq. (11). Kinetic Monte Carlo simulations were performed to calculate the Onsager transport coefficients. The dimensions of our simulation cell were $10 \times 10 \times 10$ conventional FCC cells (4000 atoms) and contained a single vacancy. The Onsager coefficients scale linearly with the vacancy concentration in the dilute vacancy limit[35], and we adjusted their values accordingly, using the equilibrium vacancy concentrations from our Grand Canonical simulations[72]. All thermodynamic and kinetic quantities were calculated at 1300 K as this value is close to the operating temperature of jet engines where Ni-Al alloys serve as the base alloy for the turbine blades[44].

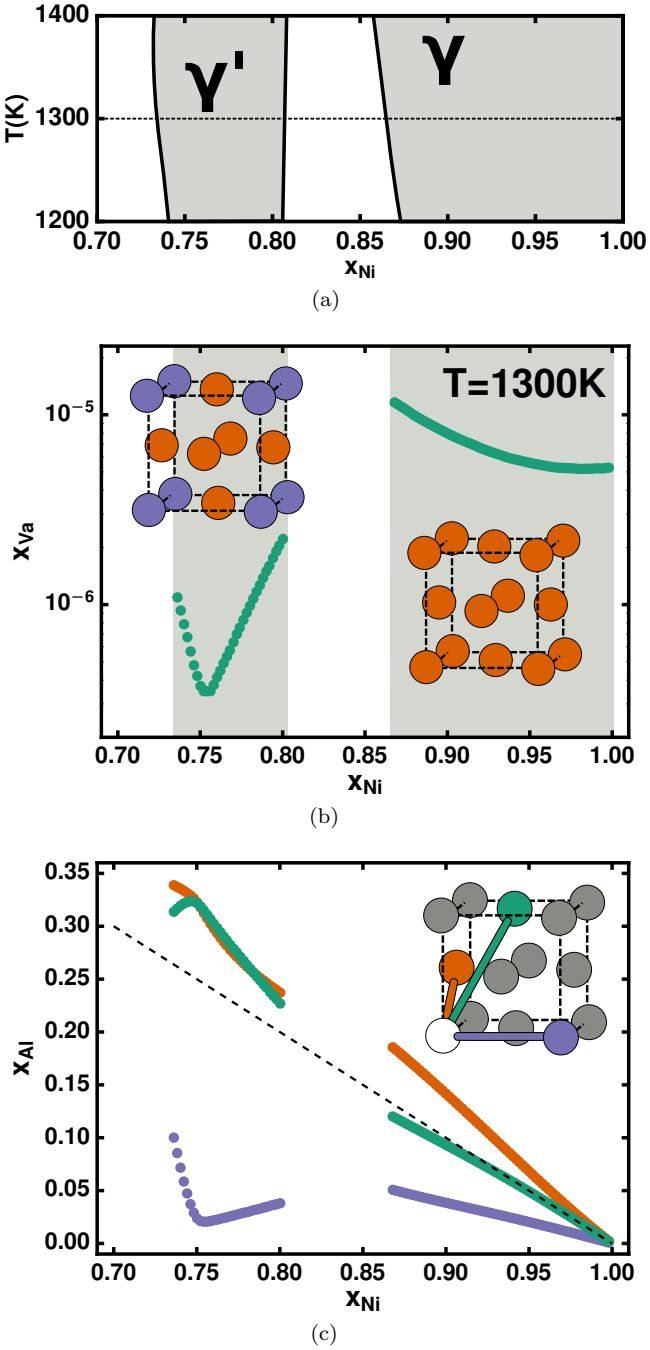

FIG. 2. Calculated thermodynamic properties of the γ and γ' phases. (a) Equilibrium phase boundaries of the Ni-rich side of the Ni-Al binary phase diagram. (b) The equilibrium vacancy concentration as a function of alloy concentration. (c) The local compositions around a vacancy in its nearest neighbor, second nearest neighbor, and third nearest neighbor shells. The alloy concentration is shown as a dashed line.

IV. RESULTS

A. Thermodynamic Properties

Figure 2a shows the calculated phase diagram of the Ni-rich FCC portion of the Ni-Al binary. The shaded areas represent single phase regions corresponding to the γ and γ' phases. The γ phase is a Ni-rich disordered solid solution on FCC while the γ' phase is an $L1_2$ ordering with an ideal stoichiometry of Ni_3Al. The calculated phase diagram shows that γ' is stable over a wide composition range, with off-stoichiometry accommodated by Ni anti-site defects for Ni rich compositions and Al anti-site defects for Al compositions[43].

Figure 2b shows the equilibrium vacancy concentration as a function of alloy composition calculated at 1300 K. The vacancy concentration clearly depends both on the overall alloy concentration and the degree of ordering, exhibiting a strong dip at the stoichiometric Ni_3Al composition of γ'. Figure 2c shows the average Al concentration of the nearest, next nearest and third nearest neighbor shells of a vacancy. Our DFT calculations predict that Al has an energetic preference to occupy the nearest neighbor shell of a vacant site in a Ni rich supercell, while the converse is predicted for the second nearest neighbor shell. This is faithfully reproduced by the ternary cluster expansion and manifests itself as an increased Al concentration within the nearest neighbor shell (orange curve in fig. 2c) and a reduced Al concentration in the second nearest neighbor shell (purple curve) of a vacancy relative to that of the average alloy (dashed line). Figure 2c also shows that the interaction between a vacancy and Al in the third nearest neighbor shell (green curve) is insufficiently strong at 1300K to produce a significant deviation from the average alloy composition.

Figure 2c reveals that the vacancy predominantly occupies the Ni sub lattice of γ' $L1_2$ ordering. A vacancy on the Ni sub lattice is exclusively surrounded by Ni in its second nearest neighbor shell. Figure 2c shows that the Al concentration in the second nearest neighbor shell of a vacancy decreases dramatically in γ', exhibiting a minimum close to the stoichiometric composition, where the number of Ni and Al anti-site defects are at a minimum. The high temperature prediction that the vacancy segregates to the Ni sub lattice of γ' is again consistent with the DFT supercell calculations of vacancy formation energies. It is also consistent with experimental positron lifetime spectroscopy measurements of Ni_3Al, which showed a tendency for thermal vacancy segregation to the Ni sublattice[73].

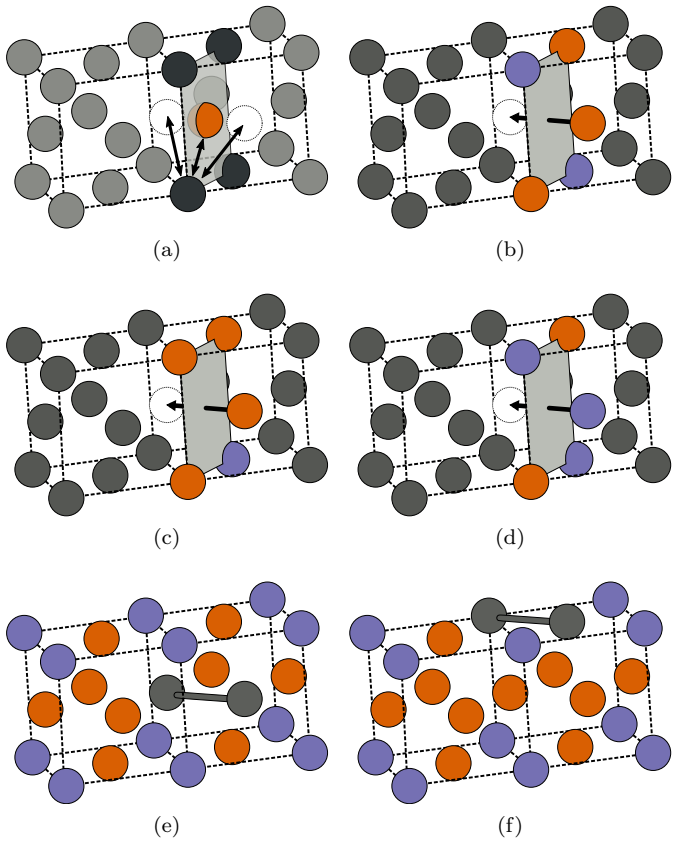

FIG. 3. (a) An atom in the activated state is closer to the ACE atoms (black) than when it is in an end state. (b)-(d) Examples of different ACE environments. Ni atoms are shown in orange, Al is colored purple and vacancies are white. In the $L1_2$ ordering, hops can occur between two Ni sublattices (e), or between an Al and a Ni sublattice (f).

B. Migration Barriers

We explore the dependence of migration barriers on local environment. It is useful to distinguish two regions surrounding a hop when assessing the role of the local environment on migration barriers. The first corresponds to the shell of atoms that directly coordinate the activated state. In FCC, an atom moving into a nearest neighbor vacancy must pass through a rectangle of four atoms, as shown in fig. 3. We refer to this shell of sites as the Activated Coordination Environment (ACE). The second region consists of all other sites outside the ACE and the hop cluster.

The decoration on the ACE should have the largest impact on the activation barrier. Figure 3 illustrates several symmetrically distinct decorations over the ACE, independent of the ordering in shells further away from the hop cluster. Atomic shells at further distances, however, will also influence the activation barrier. For example, a hop in a dilute Ni-rich solid solution and a hop in $L1_2$ may have identical Ni-Al arrangements on the ACE, but very different arrangements in the outer region. It is unlikely that these two hops will have the same activation barriers.

A Ni or Al hop in pure Ni occurs in only one distinct environment. The $L1_2$ ordering in contrast, breaks translational symmetry and thereby produces two distinct local hop environments: one between two different Ni sublattice sites, and another between an Al sublattice site and any of its nearest neighbor Ni sublattice sites. The local environments of these hops in the absence of local antisite perturbations are shown in figs. 3e and 3f. Additional local hop environments were enumerated by adding Al to the ACE of hops in pure Ni and by decorating the ACE of the two distinct hop environments in $L1_2$ with antisite defects.

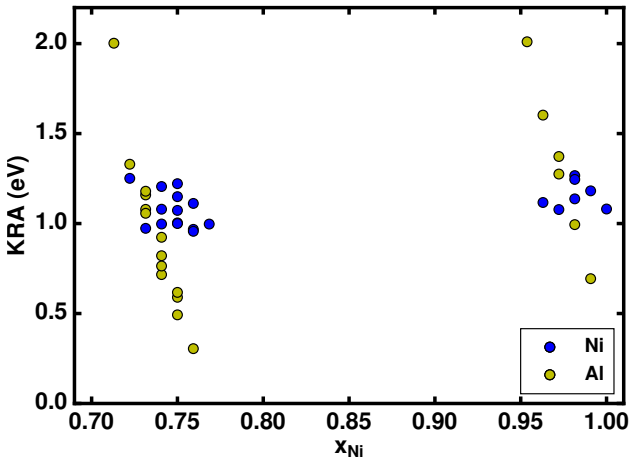

(a)

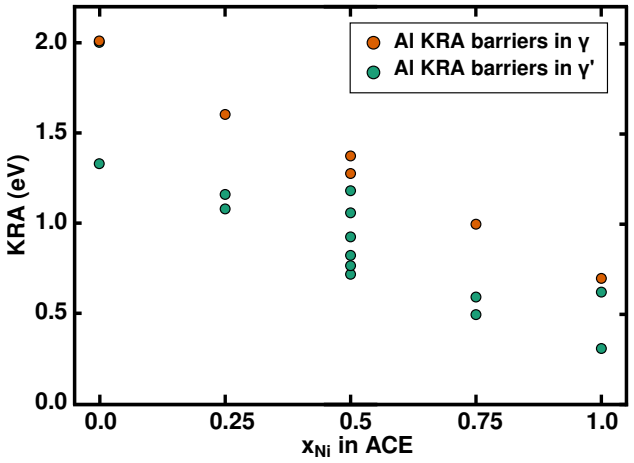

(b)

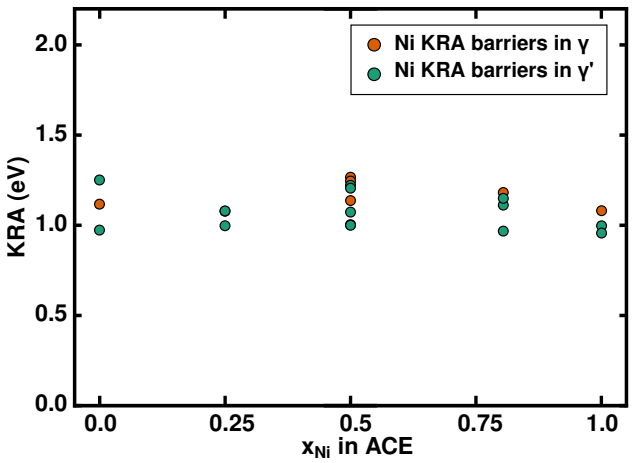

(c)

FIG. 4. (a) KRA barriers as a function of the alloy composition, with the hops colored to distinguish between Ni-Va, and Al-Va exchanges. KRA barriers as a function of the Ni composition in the ACE for (b) Al-vacancy and (c) Ni-vacancy exchanges. Colors are used to distinguish KRA barriers calculated in Ni-rich γ from those calculated in the $L1_2$ ordering.

Figure 4a shows calculated KRA barriers for Ni and Al hops as a function of alloy composition. Figures 4b and 4c show the same KRA barriers, but as a function of the Ni concentration in the ACE. There is a striking difference in the dependence of the Ni and Al KRA barriers on the ACE concentration. Regardless of local and long-range ordering, fig. 4c shows that the Ni KRA barriers remain constant to within 250meV. In contrast, fig. 4b shows a strong, almost linear dependence of the Al KRA on the ACE composition. Furthermore, long-range ordering in the crystal also impacts Al KRA barriers, as is clear from the systematic downward shift of KRA barriers for hops in $L1_2$ (green) compared to those in pure Ni (orange) for the same ACE ordering.

Two local cluster expansions, one for Ni, and another for Al KRA barriers, were constructed, using a genetic algorithm approach to select basis functions having non-zero expansion coefficients[74]. Figure 6a shows 4 different shells of sites around a nearest-neighbor hop in FCC, where each shell, having a different color, is a collection of symmetrically equivalent sites under the local hop symmetry $\mathcal{L}$. The pool of available clusters for the local cluster expansions contained up to 3-body terms consisting of any combination of sites of the 4 shells. A total of 22 Ni KRAs and 21 Al KRAs were used to train the cluster expansions. The Ni KRA cluster expansion was constructed using 4 local basis functions, and has a leave-one-out cross validation (LOOCV) score of 62meV. The Al KRA cluster expansion has a total of 5 basis functions with a LOOCV score of 69meV. Figures 6b and 6c shows the magnitudes and selected clusters of the two cluster expansions. The local cluster expansions faithfully reproduce the different trends for Ni and Al KRA barriers.

C. Transport coefficients

Figure 5a shows Onsager transport coefficients as calculated with kinetic Monte Carlo simulations using the ternary Ni-Al-Va alloy cluster expansion for the end state energies of each hop and the two local cluster expansions for the KRA barriers for Ni-vacancy and Al-vacancy hops. The Onsager coefficients scale linearly with the vacancy concentration when the vacancies are dilute[35]. The diagonal and off-diagonal coefficients, $\tilde{L}_{\mathrm{Ni,Ni}}$, $\tilde{L}_{\mathrm{Al,Al}}$ and $\tilde{L}_{\mathrm{Ni,Al}}$, exhibit a composition dependence for the γ phase that is similar to that of a thermodynamically ideal solid solution[28,35,75]. In the γ' phase both $L_{\mathrm{Ni,Ni}}$ and $L_{\mathrm{Al,Al}}$ exhibit a dip near $x_{\mathrm{Ni}} = 0.75$ due to a decrease in the equilibrium vacancy concentration and a minimum in the number of Al and Ni anti-site defects at the stoichiometric composition of the $L1_2$ ordering. The cross term $L_{\mathrm{Ni,Al}}$ becomes negative below $x_{\mathrm{Ni}} = 0.78$ (hollow circles).

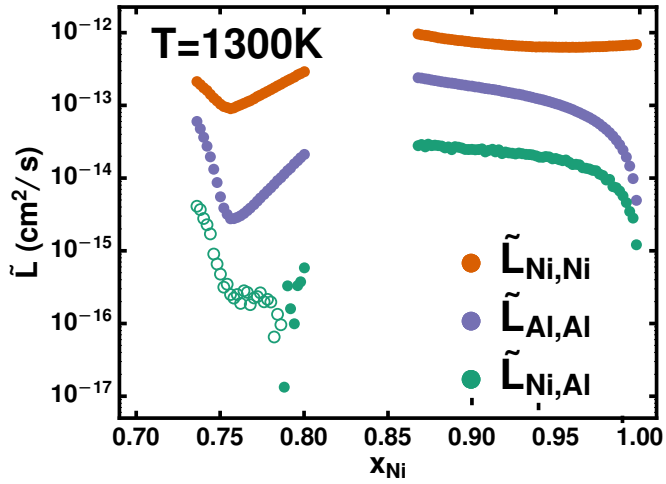

(a)

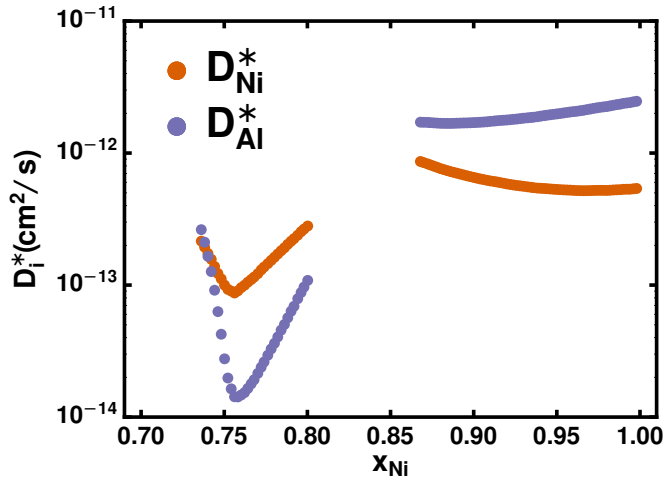

(b)

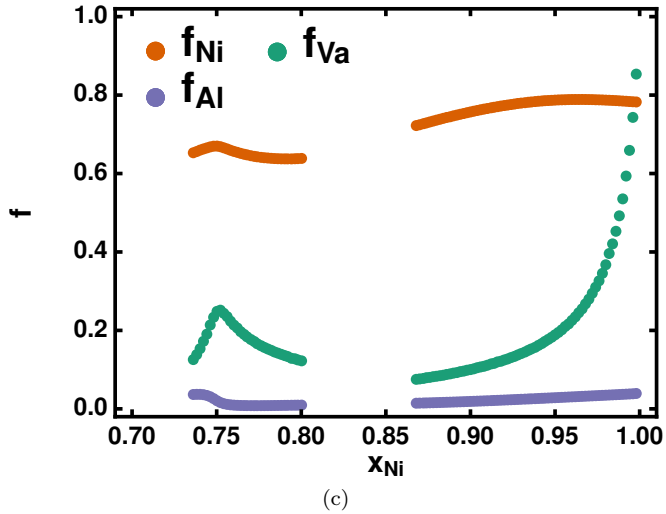

(c)

FIG. 5. (a) Onsager coefficients, (b) tracer diffusion coefficients and (c) correlation factors as calculated with kinetic Monte Carlo simulations at 1300K. The off diagonal $\tilde{L}_{\mathrm{Ni,Al}}$ in (a) becomes negative at Al rich concentrations in the γ' phase. Hollow points represent data where the absolute value of a negative $\tilde{L}_{\mathrm{Ni,Al}}$ was taken.

Further insights about diffusion mechanisms are revealed by considering tracer diffusion coefficients, which are a measure of the mobility of individual atoms in the crystal. Figure 5b shows the tracer diffusion coefficients of both Ni and Al as a function of alloy composition. The tracer diffusion coefficient of Al is higher than that of Ni in the γ phase. Al is therefore more mobile in the disordered solid solution. This can be understood by inspection of the KRA barriers for Ni and Al at dilute Al concentrations. Figure 4 shows that the KRA barrier for Al is substantially lower than that for Ni for local hop environments that are rich in Ni, as is typical for a Ni-rich disordered solid solution such as the γ phase. The relative magnitudes of the Al and Ni tracer diffusion coefficients are reversed in the γ' phase with Ni being the faster diffuser in the $L1_2$ ordering. In part this is due to the vacancy's preference for the Ni sub lattice of $L1_2$. The Ni sub lattice of $L1_2$ is fully interconnected and a vacancy can wander along this sub lattice without introducing additional disorder. This is not the case for a hop that involves an Al atom residing on the disconnected Al sub lattice as such an exchange will result in anti-site defects. Similar to the Onsager transport coefficients, the tracer diffusion coefficients also exhibit a minimum near a composition of $x_{\mathrm{Ni}} = 0.75$.

The calculated correlation factors, shown in fig. 5c, provide information about the role of short- and long-range order on diffusion mechanisms. In pure Ni ($x_{\mathrm{Ni}} = 1$), the correlation factor for Ni is equal to that of a single component FCC crystal (≈ 0.78), while that of the vacancy correlation factor approaches 1, indicating that it performs an uncorrelated random walk. The alloying of FCC Ni with Al results in additional correlations. The very low Al correlation factor signifies that its trajectories are highly correlated. The vacancy correlation factor also decreases rapidly with an increase in the Al composition in the γ phase, approaching values that are almost as low as that of Al. The Ni correlation factor, in contrast, is only negligibly affected by the addition of Al.

The low vacancy and Al correlation factors have both a thermodynamic and kinetic origin. The thermodynamics of the γ phase favors Al-vacancy pairs at concentrations that are higher than a random solid solution while the kinetics ensures that once a vacancy is next to an Al, it will perform a large number of Al-vacancy exchanges before breaking free to exchange with a surrounding Ni. These frequent back and forth Al-vacancy hops introduce a substantial amount of correlation along both the Al and vacancy hop trajectories. The Ni in contrast, because of their low hop frequencies (compared to Al), occasionally exchange with a vacancy and only after the vacancy has performed many exchanges with neighboring Al atoms such that the position of the vacancy between successive hops with a Ni is much less correlated.

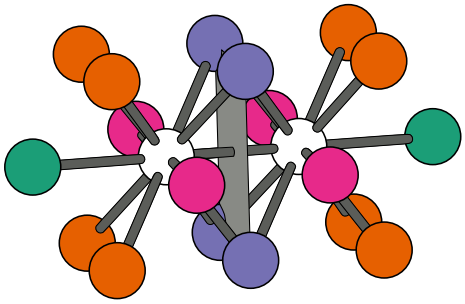

(a)

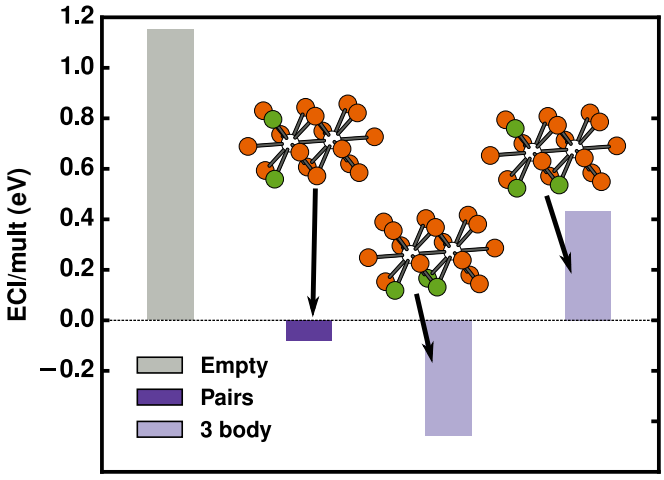

(b)

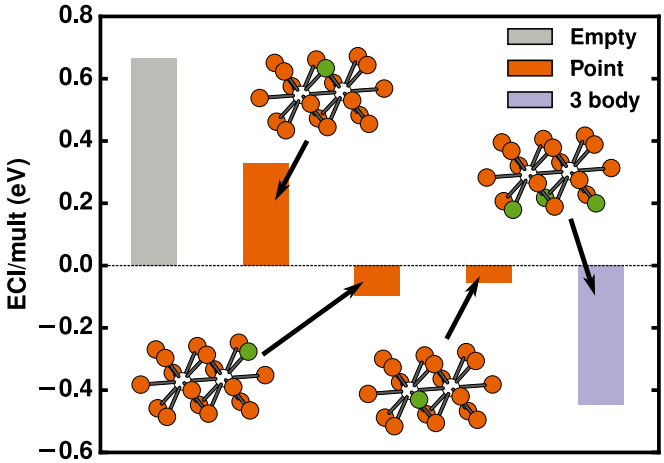

(c)

FIG. 6. (a) The local environment of a nearest neighbor hop in FCC. The end states of the hop are shown in white, while the other colors denote symmetrically equivalent sites under local symmetry. The purple sites represent the ACE. The Effective Cluster Interactions (ECI) of the local cluster expansions of the Ni and Al KRA barriers are shown in (b) and (c) respectively.

Correlated transport persists within the ordered γ' phase, as is evident in fig. 5c. However, surprisingly the vacancy correlation factor actually increases and achieves a local maximum at the stoichiometric $L1_2$ composition of $x_{\mathrm{Ni}} = 0.75$. This emerges due to the thermodynamic preference of the vacancy to reside on the fully interconnected Ni sub lattice of $L1_2$. At the stoichiometric $L1_2$ composition, the number of Al anti site defects on the Ni sub lattice is at a minimum, diminishing the chance that a vacancy encounters Al to perform large numbers of highly correlated back and forth exchanges.

The full 2×2 matrix of Fickian diffusion coefficients, $\mathbf{D}$, contains additional information about diffusion processes in the Ni-Al alloy. It embeds both thermodynamic and kinetic information as it is the product of the thermodynamic factor and the matrix of Onsager transport coefficients (eq. (9)). Rather than examining the individual elements of $\mathbf{D}$, we consider its eigenvalues[47] λ^+ and λ^-, and the diffusion metrics[35] ϕ and δ defined in eqs. (12) and (13). The larger eigenvalue λ^+ converges to the vacancy tracer diffusion coefficient in the limit of dilute vacancies. Figure 7a shows that the numerical values of λ^+ and D^*_{Va} match almost exactly. Vacancies in the Ni-Al alloy are predicted to diffuse more rapidly in the ordered γ' phase than in the disordered γ solid solution.

The smaller eigenvalue λ^- can be interpreted as an intermixing diffusion coefficient in a perfect crystal without vacancy sources and sinks.[35,47] Figure 7b shows that the intermixing diffusion coefficient is higher in γ than in γ'. Furthermore, λ^- exhibits a strong concentration dependence in γ', having a minimum at a concentration that is slightly richer than the stoichiometric $L1_2$ composition and increasing rapidly with increasing Al concentration. Also shown in fig. 7b is the inter diffusion coefficient, $\tilde{D}$, that is a measure of the rate of intermixing when there are sufficient vacancy sources and sinks to regulate an equilibrium vacancy concentration throughout the solid. These behave similarly to λ^-, especially within the γ phase.

The metric ϕ, eq. (12), tracks the bias of a vacancy flux to exchange with Al rather than with Ni. In a thermodynamically and kinetically ideal alloy, ϕ is equal to the atomic fraction of Al in the crystal[35]. Figure 7c shows that ϕ is larger than the average concentration in the γ phase, indicating a preference for vacancies to exchange with Al atoms. The opposite is true in the γ' phase, and vacancies prefer exchanging with Ni atoms, especially near stoichiometric compositions of $L1_2$.

The fourth diffusion metric δ, eq. (13), is akin to a "Kirkendall coefficient", and leads to a vacancy flux in the presence of an intermixing driving force between Ni and Al (in the absence of a vacancy flux driving force).[35] In a kinetically and thermodynamically ideal alloy $\delta = 0$, and intermixing induces no vacancy flux. The values in fig. 7d show that intermixing of Ni and Al in the γ phase causes a net vacancy flux in the "positive" direction (counter to $\vec{J}_{\mathrm{Al}}$). Since Al is the faster diffuser as revealed by the tracer diffusion coefficients, more vacancies will exchange with Al and travel in the opposite direction. Within the γ' phase, we see that Ni rich compositions lead to the opposite behavior, and intermixing causes a vacancy flux counter to Ni. For Al rich compositions, δ

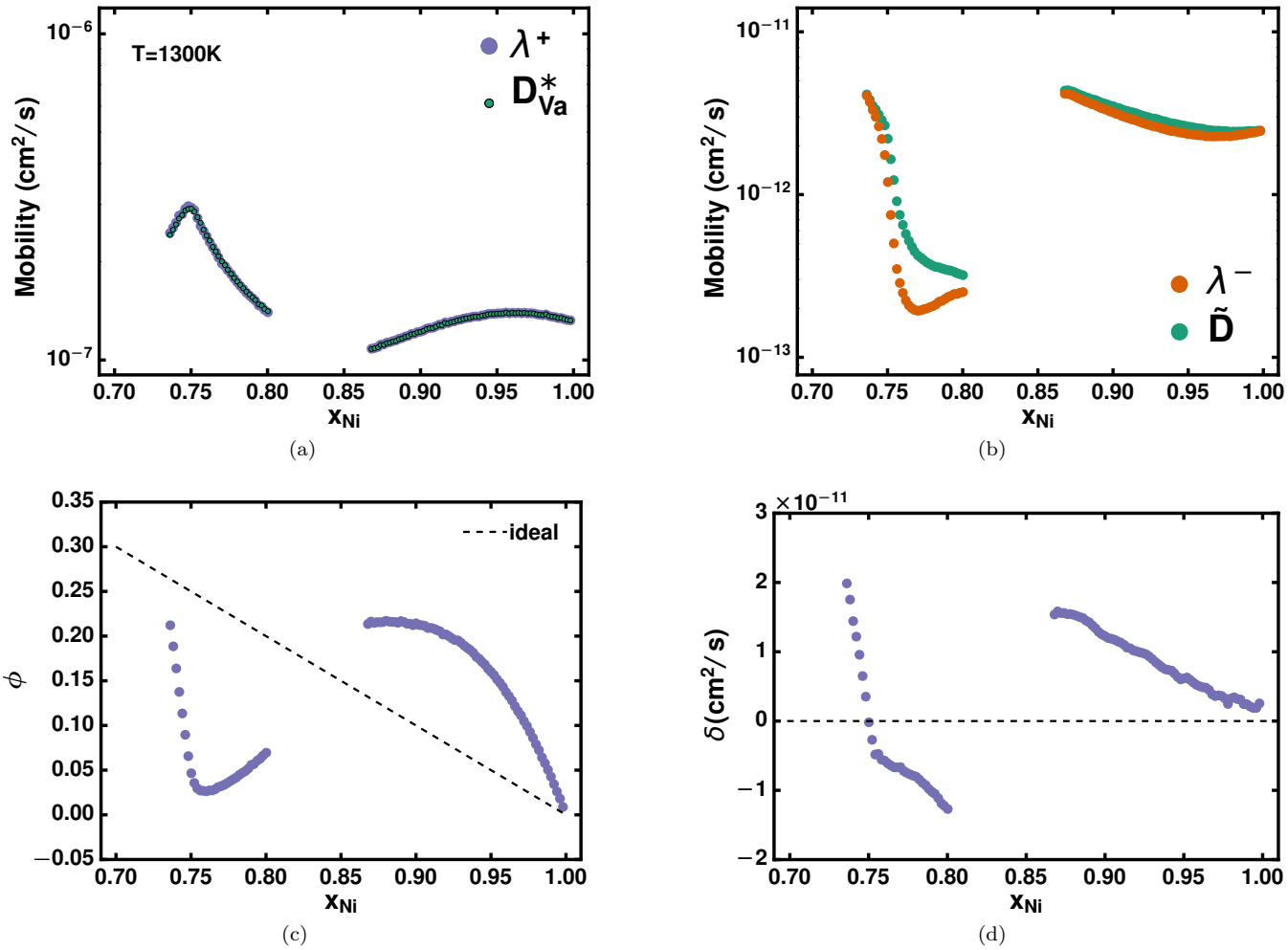

FIG. 7. (a) Comparison of λ^+ with the vacancy tracer diffusion coefficient D^*_{Va}, and (b) λ^- with the interdiffusion coefficient $\tilde{D}$ at 1300K. Values of ϕ (c) and δ (d) as a function of alloy concentration at 1300K. Dashed lines denote values for a kinetically ideal alloy.

becomes positive again. The steep rise in δ as the Al composition increases is consistent with the values of the tracer diffusion coefficients in fig. 5b, which show that Al becomes increasingly mobile as the $L1_2$ ordering becomes Al rich, even surpassing the mobility of Ni.

The trends in the calculated diffusion coefficients as a function of alloy concentration are in good qualitative agreement with experiment. While measured values for D^*_{Ni} at elevated temperatures show little to no dependence on alloy composition, experimental observations by Shi[76] and, to a lesser extent, by Hoshino[77,78], show a pronounced dip at 1173K near stoichiometric compositions of $L1_2$ Ni_3Al. Furthermore, the position of the minimum of the calculated D^*_{Ni} at $x_{\mathrm{Ni}} = 0.76$ (slightly above the stoichiometric composition of $L1_2$) is consistent with experimental measurements by Shi[76]. A similar dip was observed for In radiotracers in $L1_2$, which were used to simulate Al diffusion[76]. Measurements by Hancock[79] revealed that D^*_{Ni} is 7-10 times lower in the $L1_2$ ordered γ' phase than in pure Ni, in good agreement with calculations.

There are quantitative discrepancies between calculated and experimentally measured diffusion coefficients, with tracer and interdiffusion coefficients being systematically underpredicted by an order of magnitude compared to their experimental counterparts. Several sources for the quantitative discrepancies can be identified. While systematic errors in calculated vacancy formation energies and migration barriers may be one source, we estimate these to be no larger than 50-100 meV based on numerical convergence tests. At 1300 K, systematic errors of this order would only affect diffusion coefficients by a factor of 2 or 3. Our calculations, have, however, neglected vibrational contributions in the determination of the equilibrium vacancy concentration, which are likely to become more important at high temperature. For example, the calculated vacancy concentration of pure Ni at 1300 K is approximately an order of magni-

tude lower than experimental values measured by Sholz as compiled by Hargather et al[80]. Diffusion coefficients scale linearly with the vacancy concentration when the vacancy concentration is dilute. We have also neglected the effect of thermal expansion, which has a tendency to reduce migration barriers as the increase in volume relieves some of the steric hindrance as an atom passes through the more constricted activated state. All migration barriers in this study were calculated at the zero Kelvin DFT volume. We expect that migration barriers calculated at larger volumes that are representative of those at 1300 K will be systematically lower than those calculated at the zero Kelvin volumes. A systematic reduction in migration barriers will result in higher calculated diffusion coefficients and further close the gap between predicted and experimentally measured diffusion coefficients. The experimental studies are also likely to measure atomic transport due to short-circuit paths, including grain boundaries and dislocation cores. Short circuit diffusion usually results in larger effective diffusion coefficients than those of single crystals.

V. DISCUSSION AND CONCLUSION

We have performed a first-principles multi-scale study of diffusion in the FCC γ and γ' phases of the Ni-Al binary using cluster expansion Hamiltonians and (kinetic) Monte Carlo simulations. Diffusion in the FCC based phases of the Ni-Al binary are dominated by nearest neighbor atom-vacancy exchanges. These hop events are strongly affected by the local concentration of the alloy and the local degree of ordering among Ni and Al. A useful metric to analyze the environment dependence on an activation barrier is the kinetically resolved activation (KRA) barrier[31]. Our systematic calculations show that the KRA barriers are very sensitive to the composition in the activation coordination environment (ACE), which consists of the sites that directly coordinate the activated state of a hop. Calculations showed that there is a striking difference between the dependence of the Ni and Al KRA barriers on local environment. For Ni hops, the KRA barriers are almost independent of the local concentration and degree of ordering. The Al KRA barriers, in contrast, depend strongly on both the composition of the ACE and on the long-range ordering of the crystal outside of the ACE. In both γ and the ordered γ' phase, the Al KRA barrier is lower than that of Ni when the ACE is composed exclusively of Ni, but increases rapidly with number of Al atoms in the ACE.

Kinetic Monte Carlo simulations have allowed us to calculate various diffusion metrics in the Ni-Al binary for the FCC γ and γ' phases. These simulations predict that Al is the faster diffuser in the γ phase, while Ni is more mobile in the long-range ordered γ' phase. The higher mobility of Al in the γ phase is due to its lower KRA barrier compared to those of Ni in Ni rich environments. The Al also attracts vacancies to its nearest neighbor shell. While this ensures that dilute Al atoms have easy access to the diffusion mediating vacancies, it also leads to highly correlated diffusion, both for Al and vacancies. The thermodynamic attraction between a vacancy and Al coupled with the low Al migration barriers in Ni-rich γ results in many back and forth exchanges that do not contribute to macroscopic transport. This manifests itself in low correlation factors for both Al and vacancies.

Diffusion in γ' is significantly altered when compared to that of γ due to important changes in thermodynamic preferences imposed by the long-range ordering of $L1_2$. Vacancies are predicted to prefer the interconnected Ni-sublattice of $L1_2$ Ni_3Al. Hops that restrict the vacancy to the Ni sublattice preserve long-range order and are, therefore, thermodynamically favored. A vacancy-Al exchange in well-ordered $L1_2$ Ni_3Al, in contrast, results in a high energy anti-site defect pair, with Al on the Ni sublattice and a vacancy on the Al sublattice. A large thermodynamic driving force is then generated to reverse the exchange, restoring Al back to its isolated sublattice and the vacancy back to its preferred sublattice. These thermodynamic preferences are sufficiently strong to render Ni more mobile than Al in γ', in spite of the fact that Al has lower KRA barriers when the ACE is exclusively occupied by Ni, as is the case when it hops away from its Al sublattice site.

The diffusion metrics λ^+, λ^-, ϕ, and δ, extracted from the diffusion matrix $\mathbf{D}$, are useful for interpreting diffusion mechanisms. While the eigenvalues λ^+ and λ^- provide information about the vacancy mobility and interdiffusion coefficients respectively, ϕ and δ measure the degree with which the alloy deviates from kinetic ideality and its susceptibility to the Kirkendall effect[35]. We have successfully calculated these metrics for Ni-rich FCC Ni-Al alloys, rigorously accounting for the effects of long and short-range order on migration barriers and hop correlations by combining cluster expansions with kinetic Monte Carlo simulations.

ACKNOWLEDGMENTS

We would like to thank Brian Puchala for his help in developing methods used to systematically enumerate unique hop environments within ordered phases.

This work was supported as part of the NSF DMREF program under grant DMR-1534264. We acknowledge support from the Center for Scientific Computing from the CNSI, MRL, NSF MRSEC (DMR-1720256), and Hewlett-Packard. This research used resources of the National Energy Research Scientific Computing Center (NERSC), a U.S. Department of Energy Office of Science User Facility operated under Contract No. DE-AC02-05CH11231.

* avdv@engineering.ucsb.edu

[1] A. Van der Ven, J. Bhattacharya, and A. A. Belak, Accounts of Chemical Research **46**, 1216 (2013).
[2] M. D. Radin, S. Hy, M. Sina, C. Fang, H. Liu, J. Vinckeviciute, M. Zhang, M. S. Whittingham, Y. S. Meng, and A. V. d. Ven, Advanced Energy Materials **7**, 1602888 (2017).
[3] A. Chroneos, B. Yildiz, A. Tarancón, D. Parfitt, and J. A. Kilner, Energy Environ. Sci. **4**, 2774 (2011).
[4] B. Puchala, Y.-L. Lee, and D. Morgan, J. Electrochem. Soc. **160**, F877 (2013).
[5] K. T. Moore, W. C. Johnson, J. M. Howe, H. I. Aaronson, and D. R. Veblen, Acta Materialia **50**, 943 (2002).
[6] Y. Ma and A. J. Ardell, Acta Materialia **55**, 4419 (2007).
[7] A. R. Natarajan, E. L. Solomon, B. Puchala, E. A. Marquis, and A. Van der Ven, Acta Materialia **108**, 367 (2016).
[8] Q. Chen, J. Jeppsson, and J. Ågren, Acta Materialia **56**, 1890 (2008).
[9] P. W. Voorhees, J Stat Phys **38**, 231 (1985).
[10] P. W. Voorhees, Annual Review of Materials Science **22**, 197 (1992).
[11] J. A. Marqusee and J. Ross, The Journal of Chemical Physics **79**, 373 (1983).
[12] T. M. Pollock, D. M. Lipkin, and K. J. Hemker, MRS Bulletin **37**, 923 (2012).
[13] M. Mantina, Y. Wang, R. Arroyave, L. Q. Chen, Z. K. Liu, and C. Wolverton, Physical Review Letters **100** (2008), 10.1103/PhysRevLett.100.215901.
[14] D. Simonovic and M. H. F. Sluiter, Phys. Rev. B **79**, 054304 (2009).
[15] M. Mantina, Y. Wang, L. Chen, Z. Liu, and C. Wolverton, Acta Materialia **57**, 4102 (2009).
[16] J. D. Tucker, R. Najafabadi, T. R. Allen, and D. Morgan, Journal of Nuclear Materials **405**, 216 (2010).
[17] D. Simonovic, C. K. Ande, A. I. Duff, F. Syahputra, and M. H. F. Sluiter, Phys. Rev. B **81**, 054116 (2010).
[18] S. Choudhury, L. Barnard, J. D. Tucker, T. R. Allen, B. D. Wirth, M. Asta, and D. Morgan, Journal of Nuclear Materials **411**, 1 (2011).
[19] S. Ganeshan, L. Hector, and Z.-K. Liu, Acta Materialia **59**, 3214 (2011).
[20] H. Ding, V. I. Razumovskiy, and M. Asta, Acta Materialia **70**, 130 (2014).
[21] S. S. Naghavi, V. I. Hegde, and C. Wolverton, Acta Materialia **132**, 467 (2017).
[22] R. Agarwal and D. R. Trinkle, Phys. Rev. B **94**, 054106 (2016).
[23] C. D. Versteylen, N. H. van Dijk, and M. H. F. Sluiter, Phys. Rev. B **96**, 094105 (2017).
[24] T. D. R, Philosophical Magazine , 1.
[25] H.-J. Lu, H. Wu, N. Zou, X.-G. Lu, Y.-L. He, and D. Morgan, Acta Materialia **154**, 161 (2018).
[26] R. Agarwal and D. R. Trinkle, Phys. Rev. Lett. **118**, 105901 (2017).
[27] M. Nastar, V. Y. Dobretsov, and G. Martin, Philosophical Magazine A **80**, 155 (2000).
[28] I. V. Belova and G. E. Murch, Philosophical Magazine A **80**, 599 (2000).
[29] I. V. Belova and G. E. Murch, Philosophical Magazine A **80**, 1469 (2000).
[30] I. V. Belova and G. E. Murch, Philosophical Magazine A **81**, 1749 (2001).
[31] A. Van der Ven, G. Ceder, M. Asta, and P. D. Tepesch, Phys. Rev. B **64**, 184307 (2001).
[32] M. Nastar and V. Barbe, Faraday Discuss. **134**, 331 (2006).
[33] A. Van der Ven and G. Ceder, Physical Review Letters **94** (2005), 10.1103/PhysRevLett.94.045901.
[34] A. Van der Ven, J. C. Thomas, Q. Xu, B. Swoboda, and D. Morgan, Phys. Rev. B **78**, 104306 (2008).
[35] A. Van der Ven, H.-C. Yu, G. Ceder, and K. Thornton, Progress in Materials Science **55**, 61 (2010).
[36] Q. Xu and A. Van der Ven, Phys. Rev. B **81**, 064303 (2010).
[37] J. Bhattacharya and A. Van der Ven, Phys. Rev. B **83**, 144302 (2011).
[38] L. Barnard, G. Young, B. Swoboda, S. Choudhury, A. Van der Ven, D. Morgan, and J. Tucker, Acta Materialia **81**, 258 (2014).
[39] P. C. W. Holdsworth and R. J. Elliott, Philosophical Magazine A **54**, 601 (1986).
[40] J. M. Sanchez, F. Ducastelle, and D. Gratias, Physica A: Statistical Mechanics and its Applications **128**, 334 (1984).
[41] D. De Fontaine, in *Solid state physics*, Vol. 47 (Elsevier, 1994) pp. 33–176.
[42] A. B. Bortz, M. H. Kalos, and J. L. Lebowitz, Journal of Computational Physics **17**, 10 (1975).
[43] J. G. Goiri and A. Van der Ven, Physical Review B **94** (2016), 10.1103/PhysRevB.94.094111.
[44] T. M. Pollock and S. Tin, Journal of propulsion and power **22**, 361 (2006).
[45] T. M. Pollock and A. S. Argon, Acta Metallurgica et Materialia **40**, 1 (1992).
[46] J. W. Cahn and F. C. Larché, Scripta Metallurgica **17**, 927 (1983).
[47] K. W. Kehr, K. Binder, and S. M. Reulein, Phys. Rev. B **39**, 4891 (1989).
[48] R. W. Balluffi, S. M. Allen, and W. C. Carter, in *Kinetics of Materials* (John Wiley & Sons, Inc., 2005) pp. 145–161.
[49] R. E. Howard and A. B. Lidiard, Reports on Progress in Physics **27**, 161 (1964).
[50] A. R. Allnatt and E. L. Allnatt, Philosophical Magazine A **49**, 625 (1984).
[51] A. R. Allnatt, The Journal of Chemical Physics **43**, 1855 (1965).
[52] A. R. Allnatt and A. B. Lidiard, *Atomic Transport in Solids by A. R. Allnatt* (1993).
[53] L. Onsager, Phys. Rev. **37**, 405 (1931).
[54] G. E. Murch, Journal of Physics and Chemistry of Solids **45**, 451 (1984).
[55] L. Darken, Transactions of the American Institute of Mining and Metallurgical Engineers **175**, 184 (1948), wOS:A1948XR33900011.
[56] G. H. Vineyard, Journal of Physics and Chemistry of Solids **3**, 121 (1957).
[57] C. P. Flynn and A. M. Stoneham, Phys. Rev. B **1**, 3966 (1970).
[58] P. Hänggi, P. Talkner, and M. Borkovec, Rev. Mod. Phys. **62**, 251 (1990).
[59] S. Kadkhodaei and A. van de Walle, J. Chem. Phys. **150**, 144105 (2019), arXiv: 1812.09599.
[60] J. M. Sanchez, Physical Review B **81** (2010), 10.1103/PhysRevB.81.224202.
[61] G. Inden, in *Phase Transformations in Materials* (Wiley-

VCH Verlag GmbH & Co. KGaA, 2005) pp. 519–581.
[62] A. Van der Ven, J. Thomas, B. Puchala, and A. Natarajan, Annual Review of Materials Research **48**, 27 (2018).
[63] J. G. Goiri and A. Van der Ven, Acta Materialia **159**, 257 (2018).
[64] G. Kresse and J. Furthmüller, Computational Materials Science **6**, 15 (1996).
[65] G. Kresse and J. Furthmüller, Phys. Rev. B **54**, 11169 (1996).
[66] G. Kresse and D. Joubert, Phys. Rev. B **59**, 1758 (1999).
[67] G. Kresse and J. Hafner, Phys. Rev. B **47**, 558 (1993).
[68] G. Henkelman and H. Jónsson, J. Chem. Phys. **113**, 9978 (2000).
[69] J. C. Thomas and A. V. d. Ven, Phys. Rev. B **88**, 214111 (2013).
[70] B. Puchala and A. Van der Ven, Phys. Rev. B **88**, 094108 (2013).
[71] "First-principles statistical mechanical software for the study of multi-component crystalline solids: prisms-center/CASMcode," (2019), original-date: 2015-09-14T04:21:07Z.
[72] A. A. Belak and A. Van der Ven, Physical Review B **91** (2015), 10.1103/PhysRevB.91.224109.
[73] K. Badura-Gergen and H.-E. Schaefer, Phys. Rev. B **56**, 3032 (1997).
[74] V. Blum, G. L. W. Hart, M. J. Walorski, and A. Zunger, Physical Review B **72** (2005), 10.1103/PhysRevB.72.165113.
[75] L. K. Moleko, A. R. Allnatt, and E. L. Allnatt, Philosophical Magazine A **59**, 141 (1989).
[76] Y. Shi, G. Frohberg, and H. Wever, physica status solidi (a) **152**, 361 (1995).
[77] K. Hoshino, S. J. Rothman, and R. S. Averback, Acta Metallurgica **36**, 1271 (1988).
[78] H. Numakura, T. Ikeda, M. Koiwa, and A. Almazouzi, Philosophical Magazine A **77**, 887 (1998).
[79] G. F. Hancock, physica status solidi (a) **7**, 535 (1971).
[80] C. Z. Hargather, S.-L. Shang, Z.-K. Liu, and Y. Du, Computational Materials Science **86**, 17 (2014).